



Studies of dielectric relaxation and impedance analysis of new electronic material: $(\text{Sb}_{1/2}\text{Na}_{1/2})(\text{Fe}_{2/3}\text{Mo}_{1/3})\text{O}_3$

Subrat Kumar Barik¹ · Suhel Ahmed¹ · Sugato Hajra²

Received: 14 December 2018 / Accepted: 13 February 2019 / Published online: 20 February 2019
© Springer-Verlag GmbH Germany, part of Springer Nature 2019

Abstract

A new polycrystalline ceramic sample of $(\text{Sb}_{1/2}\text{Na}_{1/2})(\text{Fe}_{2/3}\text{Mo}_{1/3})\text{O}_3$ is formed by cheap mixed oxide processing technique. The mass loss and the calcination temperature of the sample are optimized by thermogravimetric analysis and repeated firing. The formed sample crystallizes in the orthorhombic crystal structure at room temperature depicted from the X-ray diffraction spectra. The dielectric relaxation, impedance and modulus analysis of the sample have been analyzed in various temperature and frequency range. The dielectric parameters of the sample depend on frequency and temperature and with an increment in temperature the relaxation time falls. Impedance spectroscopy analysis predicts the association of grain and grain boundary resistance. The short and long-range mobility of the charge carriers are illustrated by the modulus plot. Ac conductivity is seen to be temperature and frequency dependent and hopping of the charge carriers is also observed at high temperature. Further, the universal power law is followed by ac conductivity mechanism.

1 Introduction

Recently, multiferroic materials with perovskite (ABO_3) structure have a promising entrant due to various applications such as integrated circuits, passive components, and acoustic sensors [1–4]. In the present era special care is being taken to replace the lead-based ceramics due to its toxicity. As an alternative, many multiferroic materials are proposed and fabricated such as TbMnO_3 , YMnO_3 , BiMnO_3 and BiFeO_3 (BFO). Among them, BFO is found to be a promising candidate due to its superior structure-related properties forming a room temperature multiferroic. Unfortunately, the practical applications or dielectric properties of BFO and BFO-based solid solutions are hindered due to high leakage current and electrical conductivity. The tailoring of the physio-chemical properties of a perovskite compound is possible by tuning the A-site (rare earth/large cation) and B-site (transition metal cation). To solve these limitations different works have been reported by partial substitution of Bi and Fe

with different elements [5, 6]. But it is found in the literature that a minimum attention is given in the complete replacement of bismuth (Bi) by same group element antimony (Sb) though they have different similarity. The perovskite compounds bearing iron have achieved greater attention as they have antiferromagnetic behaviour like orthoferrite. The multiferroic property is most widely found in large family of orthoferrite to the well known BFO [7–9]. The density-functional theory was used to predict the structural, electronic, magnetic, and ferroelectric properties of SbFeO_3 by Zhang et al. [10]. The authors synthesized SbFeO_3 and $\text{SbPbO}_{2.5}$ by co-precipitation method and concluded its potential in anode for Li-ion batteries. The obtained antimony oxides have high electrochemical capacities [11]. Dixit et al. prepared SbFeO_3 (SFO) by solid-state reaction technique which suggests high dielectric parameters, and large conductivity which is due to hopping of electrons between Fe^{2+} and Fe^{3+} or may be due to the conducting nature of Sb [12]. In SFO, ferroelectric properties are related to Sb^{3+} ions with 5 s lone pair electrons while ferromagnetic properties are related to Fe^{3+} ions with partially filled d-orbital. The poor electric and magnetic properties of SFO behave as a shortcoming in its practical utility in advanced devices. The Fe^{2+} ion contents and volatile nature of Sb^{3+} lead to poor electric property. The spirally modulated spin structure generates a low value of magnetic property. To the best of our knowledge, up to 2016, no significant work has been carried out regarding the

✉ Subrat Kumar Barik
subrat.nits@gmail.com

¹ Multifunctional Materials Laboratory, Department of Physics, National Institute of Technology, Silchar, Assam 788010, India

² Department of Electronics and Instrumentation, Siksha O Anusandhan University, Bhubaneswar 751030, India

preparation and analysis of physical properties of SbFeO_3 . In our earlier two works, namely $(\text{Sb}_{1/2}\text{Li}_{1/2})(\text{Fe}_{2/3}\text{Mo}_{1/3})\text{O}_3$ and $(\text{Sb}_{1/2}\text{Na}_{1/2})(\text{Fe}_{2/3}\text{W}_{1/3})\text{O}_3$ showed enhanced electric and magnetic properties than SbFeO_3 and BFO [13, 14]. Hence the motivation behind carrying this work is to shed light on cheap ceramic processing of $(\text{Sb}_{1/2}\text{Na}_{1/2})(\text{Fe}_{2/3}\text{Mo}_{1/3})\text{O}_3$ (further termed as SNFMO) and is further investigating the nature of relaxation and conductivity using complex modulus and impedance tool, rarely reported according to the literature available.

2 Experimental procedure

The SNFMO ceramic sample was fabricated by utilizing mixed oxide processing at high temperature. The ingredients of Sb_2O_3 , MoO_3 (M/S-Loba Chemie), Na_2CO_3 , Fe_2O_3 (M/S-Merck) with high-purity ($\geq 99.9\%$) are carefully measured and mixed in a stoichiometric ratio. Further the dry, as well as wet mixing of ingredients, was done in an agate mortar for 3 h. For checking the thermal stability of the sample, a Thermal Analyzer (Perkin-Elmer, Model: Pyris Diamond) was employed. The sample was heated from 25 to 1000 °C (heating rate—10 °C/min) in argon atmosphere. By the information obtained from the TGA, the calcination of the sample was done at 900 °C for 4 h. For crystal structure and lattice parameters, the powder X-Ray diffractometer ($\text{CuK}\alpha$, $\lambda = 1.5405 \text{ \AA}$, 2θ to 20–80 degree, scan speed of 2 degree/min) was utilized. After proper phase formation, pellets of 13 mm diameter and 2 mm thickness were compressed by applying pressure of $6 \times 10^6 \text{ N/m}^2$ and polyvinyl alcohol (PVA) binder. The green pellets were then sintered at 925 °C (optimized) for 4 h. For the characterization purpose, both sides of the pellet were smoothed by an emery paper, and then painted with silver paste which behaved as an electrode. To remove the moisture of the pellets, if any, they were heated at 150 °C for 2 h before the electrical characterization. An LCR meter (HIOKI Hi Tester-3532) is employed to study the electrical properties over a temperature range (30–400 °C) and various frequencies (50 Hz–1 MHz).

3 Results and discussion

3.1 Thermal study

The TGA of SNFMO helps to understand the thermal response of the sample in the argon atmosphere. The analysis is also useful to optimize the calcination temperature and to know the thermal stability of the compound. Figure 1 illustrates the TGA graph of SNFMO sample recorded from 25 to 1000 °C. There are two steps in the total weight loss of the compound, at first 5% weight loss at 139 °C is related

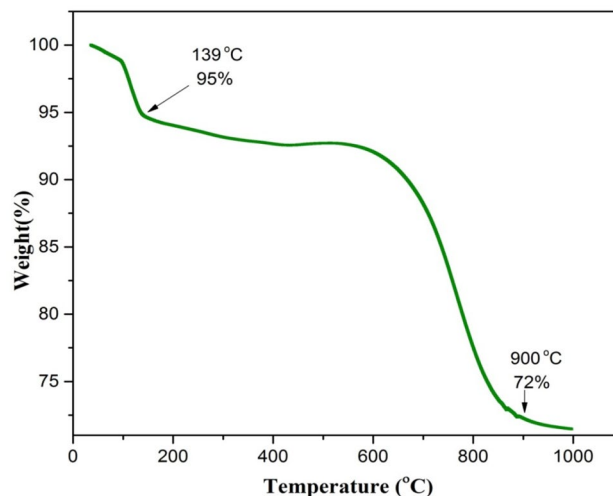


Fig. 1 Typical thermogravimetric curve of the uncalcined SNFMO mixture

to the disappearance of trapped water in the pores of the material and further 23% weight loss at 900 °C may be due to reaction among the ingredients of the sample and evolution of CO_2 gas [15]. Above 900 °C, almost zero weight loss indicates the reaction is completed forming a final product. Thus, to achieve a carbon-free product the sample is fired at 900 °C. In addition, the XRD data reveals that the proper phase formation is taken place at the same temperature.

3.2 Structural and morphology study

The X-ray diffraction (XRD) is a technique for the identification of phase purity and crystal structure. Figure 2a displays XRD pattern of SNFMO powder calcined at 900 °C. The software “POWDMULT” is used indexing of all the peaks and the lattice parameters of the sample [16]. Depending on the least deviation between them [$\sum \Delta d = \sum (d_{\text{obs}} - d_{\text{cal}}) = \text{minimum}$] the crystal structure crystallizes in orthorhombic with $a = 9.8412 \text{ \AA}$, $b = 9.2912 \text{ \AA}$, $c = 5.3097 \text{ \AA}$ (S.D. = 0.0012 Å). The Scherrer’s equation ($P_{hkl} = K\lambda/\beta_{1/2} \cos \theta$, $\beta_{1/2}$ = full width at half maximum, θ is the Bragg angle, λ is the X-Ray wavelength, K is dimensionless shape factor, with a value close to unity. The typical value of shape factor is about 0.9, but differs with the actual shape of the crystallite) helps to evaluate the crystallite size and noted to be 44 nm [17] for strong reflection peak (3 0 0). The degree of distortion from ideal perovskite structure (i.e. tolerance factor) of the sample is found to be 0.82 by Goldschmidt tolerance factor (t) relation [18]; $t = \frac{R_A + R_O}{\sqrt{2}(R_B + R_O)}$, where the symbols represent the similar meaning. The distorted perovskite structure is being suggested as there is a deviation from the ideal perovskite structure ($t = 1$).

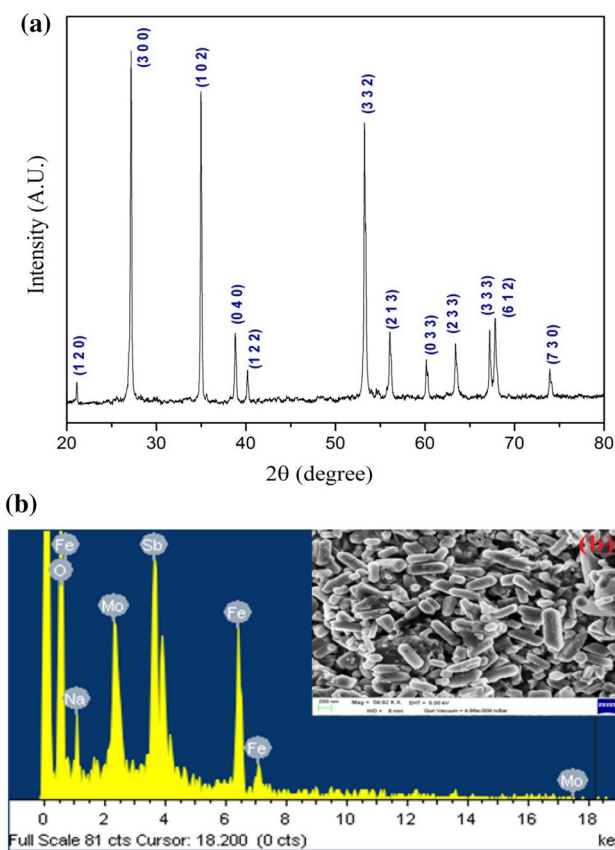


Fig. 2 a Room temperature XRD pattern of the calcined powder of SNFMO. b The energy dispersive X-ray (EDX) pattern shows the presence of elements O, Na, Fe, Mo and Sb. Inset figure shows the surface micrograph of sintered SNFMO pellet

Table 1 Atomic % and weight % as found in EDX spectra

Element	Weight %	Atomic %
O	31.77	67.93
Na	4.96	7.37
Sb	33.74	9.48
Fe	18.32	11.22
Mo	11.21	4.00
Total	100	

Figure 2b inset presents the nature of the surface microstructure of SNFMO specimen. There is a close packing of grains of various sizes over the entire surface of the studied ceramic compound with few voids. The energy dispersive X-ray (EDX) helps to compositionally verify the samples and the reflections corresponding to particular elements in the sample is obtained. Figure 2b presents the EDX pattern showing the presence of elements O, Na, Fe, Mo and Sb. The percentage of weight and number of atoms of the different elements present in the compound are presented in Table 1.

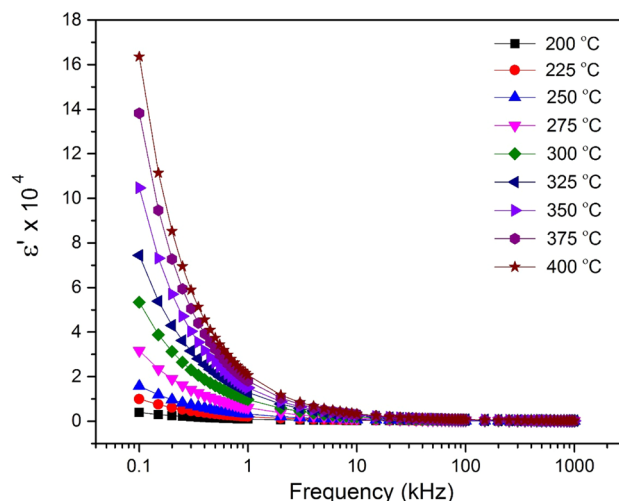


Fig. 3 Frequency dependence of dielectric constant (ϵ') at selected temperature

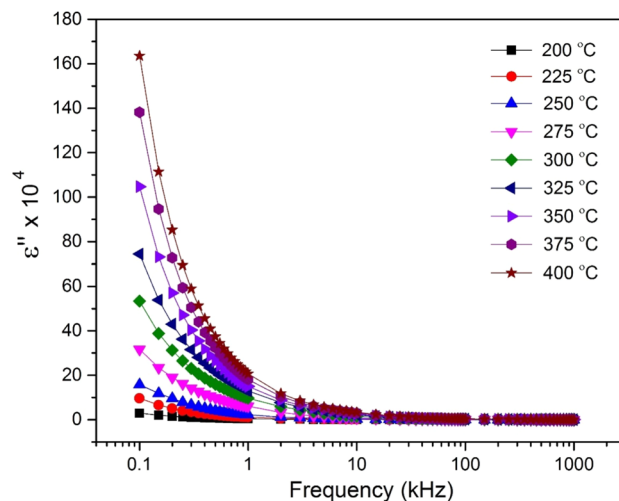


Fig. 4 Frequency dependence of dielectric loss (ϵ'') at selected temperature

The stoichiometric composition of the prepared material is again verified with the help of EDX spectra which is similar to the base composition and free from impurity.

3.3 Dielectric study

The dielectric analysis of SNFMO has been carried out to identify the types of polarizations responsible in the dielectric relaxation and the factors responsible for the dielectric loss. Figures 3 and 4 depict the variation of dielectric constant (ϵ') and loss factor (ϵ'') with frequency at few temperatures. From the figure it is observed that ϵ' decreases with enhancement in frequency. This may be due to (i) the

dielectric constant of a sample is directly related to polarization and the polarization is related to the separation of charge species. It is seen at low frequency space charges have enough time to follow the applied electric field, but at high frequency they fail to follow the same and hence polarization falls which in turn decrease the dielectric constant [19], (ii) the dielectric constant is inversely proportional to the conduction of the sample. The hopping of the electrons from Fe²⁺ to Fe³⁺ ions require very large energy, at low frequency due to low energy they do not move, but at high frequency they find enough energy and hopping mechanism starts and thus conduction increases which reduces the dielectric constant [20]. Variation of ϵ'' with frequency and temperature follows the same pattern as that of ϵ' . The reason for the dielectric loss, i.e. dissipation of energy is due to the combined effect of resistive and relaxation loss. The resistive loss in the compound is due to the consumption of energy by the mobile charge carriers and relaxation loss is the loss of energy due to the relaxation of charge carriers. Further, both ϵ' and ϵ'' enhance with increment in temperature at low frequency and at high frequency it is temperature independent. This may be due the fact that at low frequency, temperature-dependent dipolar and space charge polarization are present while at high frequency electronic and ionic polarization are dominant [21, 22].

3.4 Impedance study

Figure 5 illustrates the change of the real part of impedance with frequency at selected temperatures. From the figure following observations and conclusions can be drawn; (i) the value of Z' reduces with temperature and frequency which indicates the rise of ac conductivity [20], (ii) Z' merges at

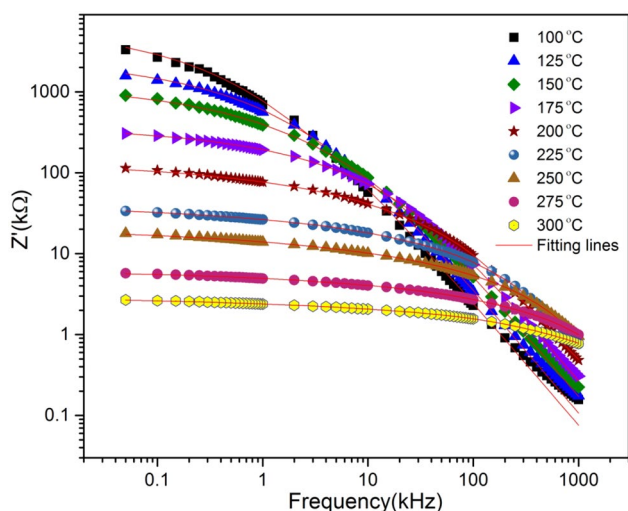


Fig. 5 Variation of real part of impedance (Z') as a function of frequency at different temperature

high frequency may be due to release of space charge and consequently lowering the barrier potential [21], (iii) at low frequency regime, Z' do not depend on frequency which predicts the existence of dc conductivity [22], (iv) at high frequency, Z' depend on frequency which suggests the presence of ac conductivity in the prepared material [22].

Figure 6 illustrates the change of the imaginary part of impedance (Z'') with frequency at different temperature. The Z'' value monotonously falls with the rise of temperature and frequency at a low temperature region (graph is not shown) without any peak which means that the capacitive resistance of the sample falls with temperature and frequency [23]. This decreases of Z'' leads to the rise of the ac conductivity in the prepared specimen. From the figure it is observed that (i) at high temperature (≤ 100 °C) the peaks appeared show relaxation phenomena in the sample, (ii) the peaks are suppressed with increases in temperature indicating that relaxation phenomena is temperature dependent, (iii) the peaks are shifted towards high frequency with temperature rise predict that the relaxation time falls with rise in temperature, (iv) at very high frequency the curves merges with each other which may be due to release of space charges. The relaxation species are space charges or immobile species at lower temperatures while at high temperature, vacancies or defects act as same [24].

One of the best ways to understand the electric response of a material is the Nyquist plot. We have plotted the imaginary part of impedance against the real part of impedance of SNFMO to separate the grain (G) and grain boundary (GB) contribution of the material responsible in the conduction process. Figure 7 represents the Nyquist plots of SNFMO at different temperatures (175–250 °C). The plot displays single semicircular arc up to 175 °C which signatures the

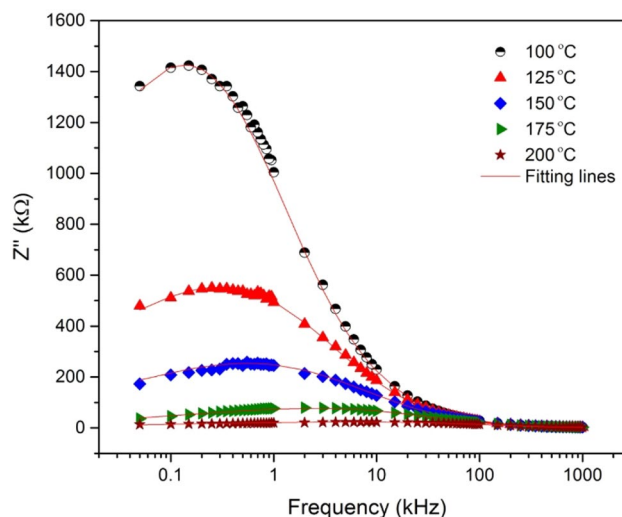


Fig. 6 Variation of imaginary part of impedance (Z'') as a function of frequency at different temperature

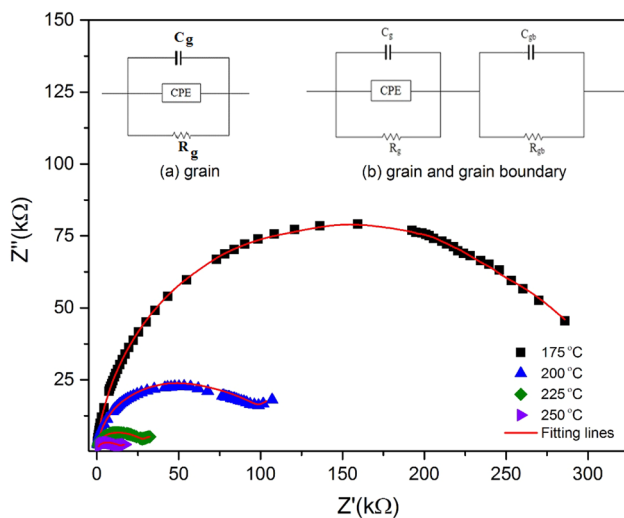


Fig. 7 Nyquist plots of SNFMO at different temperatures. Figure (inset) shows the schematic equivalent electric circuits correspond to the (a) grain, (b) grain and grain boundary effect of SNFMO

presence of grain effect and two semicircular arcs start from 200 °C indicate the association of G and GB effect. All the semicircles are depressed suggests the relaxation phenomena of sample is non-Debye type [25]. The factors involved are grain orientation, atomic defect distribution and stress-strain phenomena [26]. The interlope of each semicircular arc on the Z' axis gives the resistive component of the sample. To identify the relaxation mechanism, complex impedance data is simulated with the suitable electric circuit shown in Fig. 7 (inset). The G response can be represented by the parallel combination of (RQC) and G and GB can be represented by series connection of parallel (RQC) and (RC). R =resistance, C =capacitance and Q =constant phase element. CPE is defined as $CPE(Y) = A_0(j\omega)^n$, A_0 =exponent factor and n ($1 > n > 0$) determine the departure from the ideal Debye behavior. Q acts as capacitor when $n=1$ and when $n=0$, it acts as a resistor. The ZSIMPWIN software is utilized to fit the experimental data (symbols) with the equivalent data (solid line) and the fitting parameters are given in Table 1. The GB resistance value is lower than G resistance due to vacancies and space charge present at the GB [27]. The resistance (G and GB) reduces with temperature rise which confirms the negative temperature coefficient of resistance (NTCR) behavior of SNFMO.

3.5 Modulus study

To get a clear understanding of relaxation phenomena in SNFMO only the impedance analysis is insufficient. The impedance analysis shed light on the large resistance of the sample while the modulus study stress on the smallest capacitance of the microstructural components of the compound.

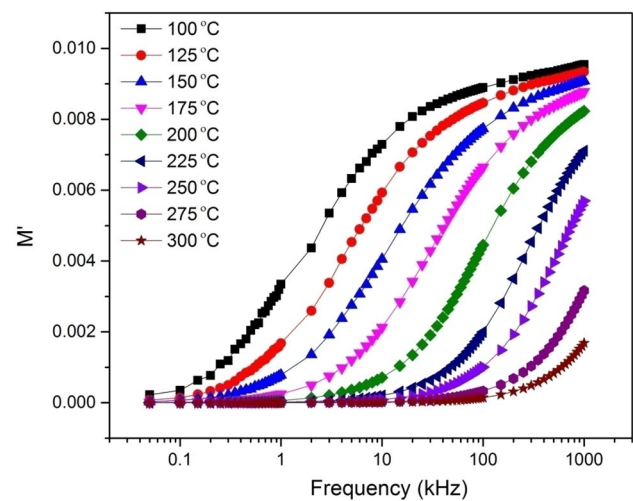


Fig. 8 Variation of real part of modulus (M') as a function of frequency at selected temperature

We have analysed the prepared sample with modulus spectroscopy to know the effect of electrode polarization, types of mobility of the charge carriers, the range of the movement of the charge carrier, the variation of the capacitance of the sample with frequency and temperature. Figure 8 illustrates the frequency dependent real part of modulus at selected temperatures. It is depicted that at low frequency all the curves appear to merge with each other which suggests the absence of electrode polarization in the sample. All the curves at high frequency merge with each other reveal the absence of space polarization which is also observed in the dielectric and impedance analysis. M' rises with frequency and finally attains a constant value at very high frequency. This indicates that the movement of the charge carriers is not governed by the restoring force and hence they can move over the long range [28]. Also the sigmoidal increase of M' predicts the short-range mobility of the charge carriers [28]. Thus, the analysis predicts the existence of both short range and long range movement of the charge carriers in the prepared sample.

To identify the regions where the charge carriers are mobile in short range and long range, the variation of imaginary part of the modulus (M'') with frequency at different temperature of SNFMO has been performed and shown in Fig. 9. The plots show the appearance of peaks which shifted with temperature. The appearance of peaks confirms the presence of relaxation phenomena. The peaks shifted towards the high-frequency side with an increase in temperature indicate the relaxation phenomenon is temperature dependent. The charge carriers are mobile over the long-range below the peak frequency while they are confined in potential wells and can move only in short range at above the peak frequency [29]. At a peak frequency, the movement of

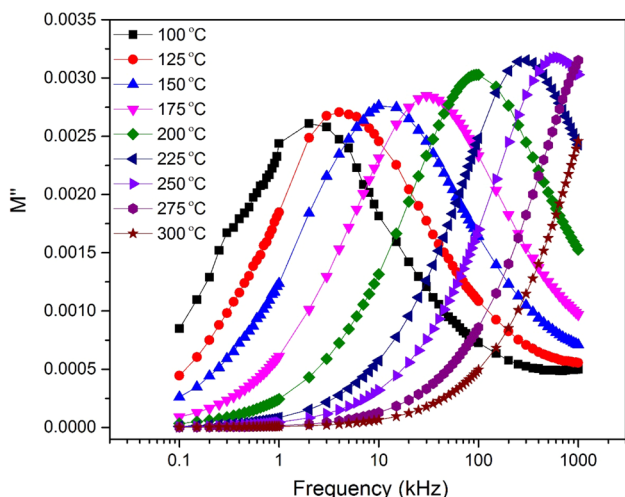


Fig. 9 Variation of imaginary part of modulus (M'') as a function of frequency at selected temperature

the charge carriers changed from long range to short range. According to J.R. Macdonald, the peak height of a sample is inversely related to the capacitance [29]. In the present sample, the peak height slightly increases with temperature, suggesting the decrease of capacitance with the rise of temperature.

From the above analysis, it is observed that both localized (short range) and non-localized (long range) movement of the charge carriers exist in the SNFMO. To confirm the same, we have plotted the frequency dependence of normalized peaks (M''/M''_{max} and Z''/Z''_{max}) measured at 150 °C as shown in Fig. 10. According to the reports, if the peaks overlap it means the non-localized mobility of the charge carriers and if they do not overlap it means both localize and

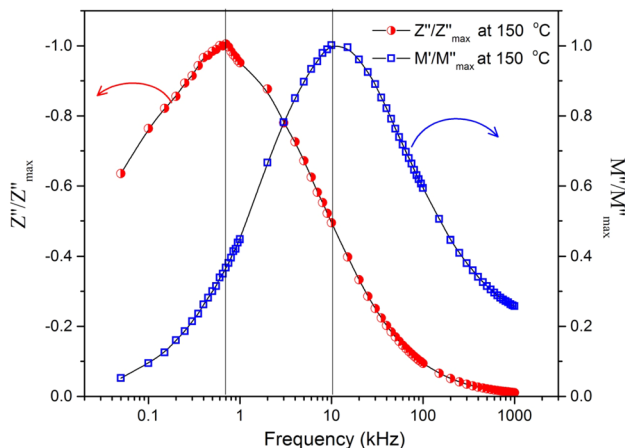


Fig. 10 Normalized plots of electric modulus M''/M''_{max} and impedance Z''/Z''_{max} of SNFMO sample as a function of frequency at 150 °C

non-localize conduction of the charge carriers [30]. A clear separation between the peaks is observed from the figure which confirmed the presence of both localized and non-localized movement of the charge carriers in SNFMO.

To understand if the spreading of relaxation time is dependent on temperature or not, the scaling behavior, i.e. M''/M''_{max} vs. $\log(ff_{max})$ of SNFMO at few temperatures is illustrated in Fig. 11. It is observed that various temperatures curve coincide into a single master curve. This reveals that in the investigated temperature range the dynamic process of relaxation is presided over by the similar relaxation mechanism with same activation energy [31]. The spreading of relaxation time is temperature independent.

To confirm the similar types of charge carriers responsible for conduction (localized/non-localized) in SNFMO, we have plotted the change of relaxation time (calculated from impedance and modulus analysis) with temperature in Fig. 12. It is observed that the relaxation time falls with temperature indicating that the relaxation phenomena are thermally activated process. Both the relaxation phenomena are analyzed by Arrhenius relation (AR): $\tau = \tau_0 \exp(-E_a/K_B T)$ where symbols have the same meaning. In the figure, the symbols correspond to experimental data and the line represents the fitting data with Arrhenius relation. The activation energy evaluated from impedance and modulus plot is 0.65 eV and 0.66 eV, respectively. The localized conduction is represented by activation energy obtained from the Z'' spectra while the non-localized conduction corresponds activation energy obtained from the M'' spectra. Since both the activation energy is same, hence similar types of charge carriers are responsible for both localized and non-localized conduction mechanism [31]. It is reported that first ionization of oxygen vacancies is responsible for the relaxation

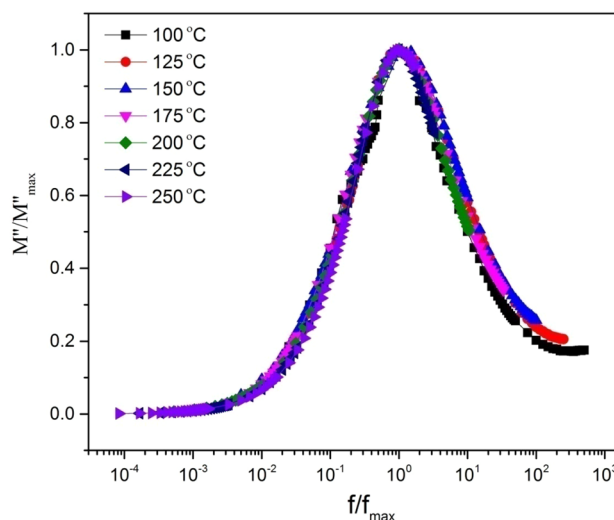


Fig. 11 Scaling behavior of M''/M''_{max} vs. $\log(ff_{max})$ for SNFMO at different temperatures

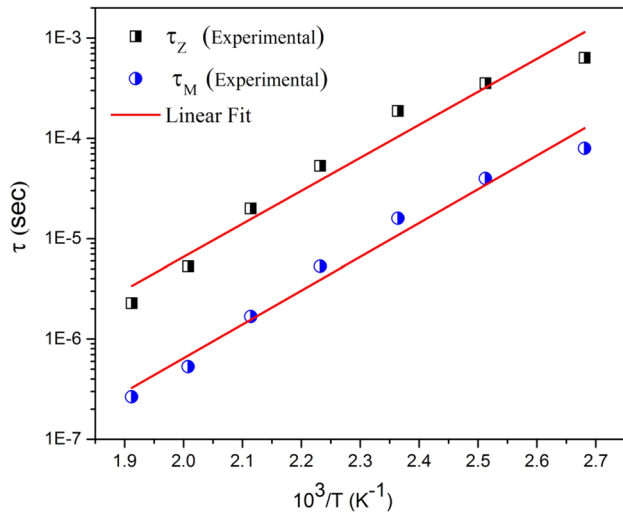


Fig. 12 Variation of relaxation time with temperature

mechanism if $E_a < 0.70$ eV and second ionization of oxygen vacancies is responsible if $E_a > 0.70$ eV [32, 33].

3.6 Dc conductivity study

The activation energy of the charge carrier in grain and grain boundary can be analyzed with the study of dc conductivity. It also predicts that which type of charge carriers are responsible for the region-oriented conduction mechanism. The expression $\sigma_{dc} = \frac{t}{RA}$ where R = grain or grain boundary resistance obtained from Nyquist plot, t = thickness of the pellet and A = area of the pellet is utilized to achieve dc conductivity. Figure 13 displays the change of dc conductivity in G and GB with inverse temperature. The conductivity in both regions, i.e. in G and GB rises with increment in

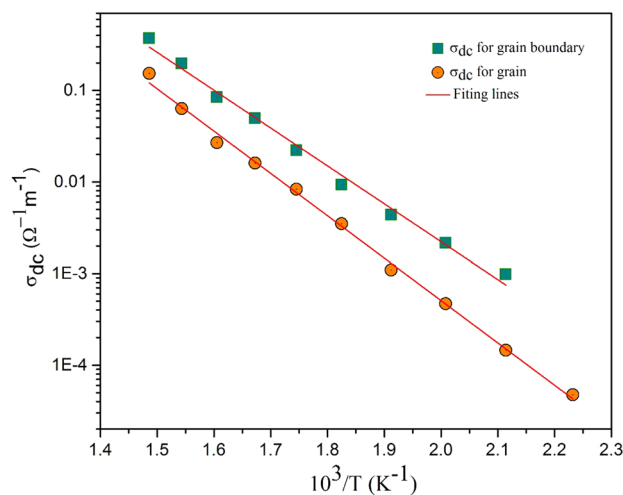


Fig. 13 Variation of dc conductivity (σ_{dc}) with inverse of temperature

temperature. This type of electrical conductivity can be explained by Arrhenius relation; $\sigma_{dc} = \sigma_0 \exp[-E_a/KT]$, where the symbols have their usual meaning. The value of activation energy in G and GB is found to be 0.82 eV for grain (175–400 °C) and 0.91 eV for GB (200–400 °C). It is noted that the charge carrier of similar kind leads to the conduction in G and GB as the activation in both the region of the sample is very near to each other. The activation energy for conduction mechanism is different to the activation energy obtained from the relaxation mechanism hence various charge carriers are responsible for conduction. The activation energy for conduction in SNFMO exceeds 0.70 eV, hence double ionization of oxygen vacancies causes the conduction mechanism.

3.7 Ac conductivity study

The frequency-dependent ac conductivity at few temperatures are shown in Fig. 14. The expression $\sigma_{ac} = \omega \epsilon_r \epsilon_0 \tan \delta$, the symbols have usual meaning used to evaluate the ac conductivity. A convenient formalism Jonscher's universal power law $\sigma(\omega) = \sigma_{dc} + A(\omega)^n$ helps to explain the variation of conductivity in SNFMO [34]. The conductivity increases with increase in frequency up to 200 °C without any change in the slope. But at temperature ≤ 225 °C, a variation in the slope of the conductivity at a particular frequency is observed which is coined to be hopping frequency. At temperature ≤ 225 °C the plots have two regions (i) the low-frequency dispersion region which is related to the ac conductivity and (ii) high-frequency plateau region is related to the dc conductivity. The low-frequency ac conduction mechanism in SNFMO is due to space charge and disordering of cations while high-frequency dc conductivity

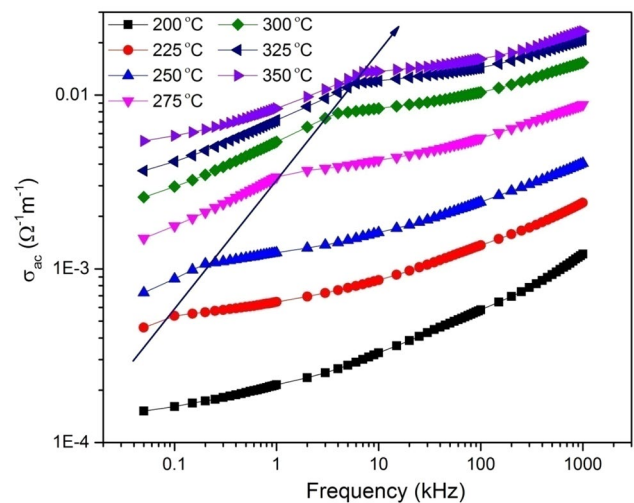


Fig. 14 Variation of ac conductivity (σ_{ac}) with frequency at different temperatures

is related to fading of space charges [35]. At hopping frequency the charge species have sufficient energy to leap over the potential barrier (grain resistance) leading to a rise in conductivity. The increase of hopping frequency with temperature indicates the decrease of potential barrier, i.e. grain resistance with the rise of temperature [35].

4 Conclusion

In summary, a polycrystalline sample SNFMO is fabricated by mixed oxide processing. Thermo gravimetric analysis of the sample displays that the material should be fired at 900 °C to get a carbon-free product. The crystal structure of the compound is orthorhombic with distorted perovskite structure. The analysis of parameters related to dielectric inferred that the permittivity and loss factor are dependent on frequency and temperature. Impedance study shows the presence of dielectric relaxation in the compound and it is dependent on temperature. The Nyquist plot shows non-Debye and NTCR behavior in SNFMO. The *G* effect of the compound takes place at ≤ 175 °C and combined *G* and GB at ≥ 200 °C. Modulus study reveals that in the present material the electrode effect is absent. The capacitance of the sample is decreasing with temperature is also predicted by modulus study. A combined electric and modulus study informed that the relaxation process is due to the single ionization of oxygen vacancies while double ionization of oxygen vacancies caused conduction mechanism. The Arrhenius-type relation and Jonscher's universal power law helps to shed light on dc and ac conductivity, respectively. The above parameters investigated to make this prepared lead-free ceramics as a budding contender towards device engineering.

Acknowledgements The authors thank AICTE for sanctioning the project [no.: 8023/RID/RPS-32/(POLICY-III)(NER)/2011-12] for experimental work.

References

- M.M. Vopson, Crit. Rev. Solid State Mater. Sci. **40**, 223–250 (2015)
- R.A.P. Ribeiro, L.H.S. Lacerda, E. Longo, J. Andrés, S.R. de Lazaro, J. Magn. Magn. Mater. **475**, 544–549 (2019)
- H.W.Y. Piaojie Xue, X. Lu, Zhu, J. Mater. Sci. Technol. **34**, 914–930 (2018)
- N.V. Minh, N.G. Quan, J. Alloys Compd. **509**, 2663 (2011)
- W. Mao, X. Li, Y. Li, X. Wang, Y. Wang, Y. Ma, X. Feng, T. Yang, J. Yang, Mater. Lett. **97**, 56 (2013)
- V.S. Puli, A. Kumar, N. Panwar, I.C. Panwar, R.S. Katiyar, J. Alloys. Compd. **509**, 8223 (2011)
- A. Scrimshire, A. Lobera, A.M.T. Bell, A.H. Jones, I. Sterianou, S.D. Forder, P.A. Bingham, J. Phys. Condens. Matter. **30**, 105704 (2018)
- N. Ramu, K. Meera, R. Ranjith, R. Muralidharan, Mater. Res. Express **6**, 036106 (2019)
- Z.-Q. Wang, Y.-S. Lan, Z.-Y. Zeng, X.-R. Chen, Q.-F. Chen, Solid State Commun. **288**, 10–17 (2019)
- G.B. Zhang, Y.X. Wang, F.Z. Ren, Y.L. Yan, J. Phys. Soc. Jpn. **81**, 074702 (2012)
- C.X. Lu, J.Y. Chu, Y.C. Zhai, Y.W. Tian, J. Harbin Inst. Technol. **36**, 10 (2004)
- S.K. Bera, S.K. Barik, R.N.P. Choudhary, P.K. Bajpai, Bull. Mater. Sci. **35**, 47 (2012)
- S. Thakur, O.P. Pandey, K. Singh, Ceram. Int. **40**, 16371 (2014)
- S. Ahmed, S.K. Barik, J. Alloys. Compd. **626**, 292 (2015)
- J.M. Luiz, J.R. Matos, I. Giolito, M. Ionashiro, Thermochim. Acta **254**, 209 (1995)
- E. Wu, J. Appl. Cryst. **22**, 506–510 (1989)
- K. He, N. Chen, C. Wang, L. Wei, J. Chen, Cryst. Res. Technol. **53**, 1700157 (2018)
- V.M. Goldschmidt, Die Geseze der Krystallochemie, Naturwissenschaften **14**, 477 (1926)
- K. Parida, R.N.P. Choudhary, Mater. Res. Express **4**, 076302 (2017)
- T. Md, M. Rahman, C.V. Vargas, Ramana, J. Alloy. Compd. **617**, 547–562 (2014)
- K. Parida, S.K. Dehury, R.N.P. Choudhary, Phys. Lett. A **380**, 4083–4091 (2016)
- C.G. Koops, Phys. Rev. **83**, 121 (1951)
- S. Nath, S.K. Barik, S. Hajra, R.N.P. Choudhary, J. Mater. Sci. Mater. Electron. **29**, 12251–12257 (2018)
- H.O. Rodrigues, G.F.M. Pires Jr., J.S. Almeida, E.O. Sancho, A.C. Ferreira, M.A.S. Silva, A.S.B. Sombra, J. Phys. Chem. Solids **71**, 1329 (2010)
- Y.K. Jun, W.T. Moon, C.M. Chang, H.S. Kim, H.S. Ryu, J.W. Kim, K.H. Kim, S.H. Hong, Solid State Comm. **135**, 133 (2005)
- S. Pattanayak, R.N.P. Choudhary, P.R. Das, J. Mater. Sci. Mater. Electron. **24**, 2767 (2013)
- X.J. Xi, S.Y. Wang, W.F. Liu, H.J. Wang, F. Guo, X. Wang, J. Gao, D.J. Li, J. Magn. Magn. Mater. **355**, 259 (2014)
- X.J. Xi, S.Y. Wang, W.F. Liu, H.J. Wang, F. Guo, X. Wang, J. Gao, D.J. Li, J. Alloys. Compd. **603**, 224 (2014)
- Y.A. Chaudhari, A. Singh, C.M. Mahajan, P.P. Jagtap, E.M. Abuassaj, R. Chatterjee, S.T. Bendre, J. Magn. Magn. Mater. **347**, 153 (2013)
- J. Mohanty, P. Behera, S.R. Mishra, T. Badapanda, S. Anwar, I.O.P. Conf. Ser. Mater. Sci. Eng. **178**, 012014 (2017)
- B. Pati, R.N.P. Choudhary, P.R. Das, Ceram. Int. **40**, 2201 (2014)
- A. Kumar, R.N.P. Choudhary, B.P. Singh, A.K. Thakur, Ceram. Int. **32**, 73 (2006)
- V. Purohit, R. Padhee, R.N.P. Choudhary, J. Mater. Sci. Mater. Electron. **29**, 5224–5232 (2018)
- S.K. Barik, R.N.P. Choudhary, P.K. Mahapatra, J. Alloys. Compd. **459**, 35 (2008)
- D.K. Pradhan, R.N.P. Choudhary, C. Rinaldi, R.S. Katiyar, J. Appl. Phys. **106**, 024102 (2009)

Publisher's Note Springer Nature remains neutral with regard to jurisdictional claims in published maps and institutional affiliations.